PHYSICAL REVIEW C **75**, 064318 (2007)

# Classical and quantum properties of the semiregular arc inside the Casten triangle

Michal Macek, Pavel Stránský, and Pavel Cejnar
*Faculty of Mathematics and Physics, Charles University, V Holešovičkách 2, CZ-18000 Prague, Czech Republic*

Stefan Heinze and Jan Jolie
*Institute of Nuclear Physics, University of Cologne, Zülpicherstrasse 77, D-50937 Cologne, Germany*

Jan Dobeš
*Nuclear Physics Institute, Academy of Sciences of the Czech Republic, CZ-250 68 Rez, Czech Republic*

(Received 23 November 2006; published 22 June 2007)

We investigate classical and quantum signatures of increased regularity in the Alhassid-Whelan semiregular arc inside the symmetry triangle of the interacting boson model. A significant bunching/antibunching pattern of quantum levels, similar to that observed along the O(6)-U(5) transition, is found in the $0^+$ energy spectrum and related to a crossover of two specific families of classical regular orbits slightly above $E = 0$. We also discuss the degeneracy of $\beta$ and $\gamma$ bandheads in a region close to the arc and the relation to regularity in the geometric model.

DOI: 10.1103/PhysRevC.75.064318 PACS number(s): 21.60.Fw, 21.60.Ev, 05.45.Mt, 21.10.Re

## I. INTRODUCTION

The interacting boson model (IBM) of nuclear collective motions, developed by Iachello and Arima [1] in the 1970's, displays a wide variety of interesting features. Apart from being successful in the description of low-lying collective states of even-even nuclei, it has also served as a useful "toy model" to study various general phenomena, such as quantum phase transitions [2–4] or order/chaos coexistence [5–16]. The interplay between regular and chaotic behaviors, observable on both the quantum and classical levels of the model, is surely one of the most intriguing properties. It seems to be a common feature of nuclear collective motions in general. The present paper contributes to this subject, extending our recent study [17,18] of fully regular dynamics in the IBM. Special attention is payed to the semiregular region of Alhassid and Whelan [8–10] lying within the parametric space of IBM.

The onset of chaos in a system is closely connected with the breakdown of symmetries [19–21]. The IBM is known [1] to possess three standard dynamical symmetries, namely, U(5), O(6), and SU(3), and two additional ones, $\overline{\mathrm{O}(6)}$ and $\overline{\mathrm{SU}(3)}$, following from gauge transformations [22]. They are related to the possible decompositions of the spectrum generating group U(6) into subgroup chains that contain the invariant-symmetry group O(3) of physical rotations. An important consequence of dynamical symmetries is the integrability of the corresponding Hamiltonians, guaranteed by the complete set of constants of motion provided by Casimir operators of respective subgroup chains [23]. The system in such cases exhibits completely regular dynamics.

Apart from the dynamical-symmetry limits, there exists a unique integrable transition path between O(6) and U(5) marked by conservation of the Casimir invariant of the common subgroup O(5) [24]. Away from these integrable regions, the IBM dynamics was expected to be chaotic until the study in Ref. [8] revealed surprisingly high degree of regularity along a particular path inside the model parameter space. This path forms a bent curve in between the SU(3) and U(5) vertices of the symmetry triangle and is called hereafter the "AW arc". Unlike the O(6)-U(5) path [15,17,18], the dynamics within the AW arc is not completely regular, indicating the existence of a kind of partial dynamical symmetry [25]. Interestingly, evolutions of energy spectra along the two regular paths display certain similarity, as we will show below.

Unknown nature of regularity along the AW arc stimulated research of the IBM properties from various perspectives. Originally, Alhassid and Whelan observed the dependence of both short- and long-range spectral correlations together with classical measures of chaos on the angular momentum $l$ and two control parameters $\eta$, $\chi$ that change the amount of dynamical symmetries in the Hamiltonian. Significant rise of regularity in the arc was found using both quantum and classical measures [8–10]. Later, the analysis of wave function entropies [26] revealed an increased localisation of energy eigenstates in dynamical-symmetry bases within a region coinciding with the AW arc. Recently, several real nuclei were located very close to the arc, an approximate degeneracy of $0_2^+$ and $2_2^+$ states being pointed out as a characteristic feature of nuclei in this region [27]. Also a close relative of the IBM—the geometric collective model (GCM)—was found to show a similar increase of classical regularity away from integrable regimes [28–30].

The layout of this article is as follows. The IBM and its classical limit are briefly described in Sec. II. In Sec. III we demonstrate increased regularity of the dynamics within the AW arc using the nearest neighbor spacing distribution of $0^+$ states and classical measures based on Poincaré sections [19] and so-called alignment indices [31]. Section IV presents an observation of strong level bunchings in the spectra of $0^+$ states along the arc, slightly above zero absolute energy. The pattern shows great degree of similarity to the bunching found in spectra along the O(6)-U(5) transition [17]. In Sec. V, we search for related effects in the classical phase space, exploiting the connection of level density with periodic orbits.

0556-2813/2007/75(6)/064318(13)

In Sec. VI we apply the technique of intrinsic states to explain the approximate degeneracy of $0_2^+$ and $2_2^+$ states close to the arc. Section VII is devoted to the comparison of regular dynamics within IBM and GCM. Finally, Sec. VIII brings a summary and outlook.

## II. HAMILTONIAN

The interacting boson model describes low-lying spectra of even-even nuclei in terms of an ensemble of $N$ bosons $s$ and $d$ with angular momenta 0 and 2, respectively. Bilinear products of creation and annihilation operators $b_i^\dagger b_j$, where $i, j = s, 1, \ldots, 5$ stand for the $s$-boson and the five components of $d$-boson, form a set of U(6) generators. We limit our investigation to the simplest version of the model, the IBM-1, which does not distinguish neutron and proton types of bosons (we use nevertheless the common abbreviation IBM). Instead of the most general quantum Hamiltonian with all rotationally invariant one- and two-body terms we consider a simplified form

$$\hat{H} = a\left[\frac{\eta}{N}\hat{n}_d - \frac{1-\eta}{N^2}(\hat{Q}_\chi \cdot \hat{Q}_\chi)\right], \tag{1}$$

with $\hat{n}_d = (d^\dagger \cdot \tilde{d})$ denoting the $d$-boson number operator and $\hat{Q}_\chi = [s^\dagger\tilde{d} + d^\dagger\tilde{s}]^{(2)} + \chi[d^\dagger\tilde{d}]^{(2)}$ the quadrupole operator. The scaling factor $a$ sets an effective energy unit in quantum spectra. In the figures below we use a numerical value $a = N/10$ in arbitrary units, thus the quantum energy is taken as an extensive quantity. Hamiltonian in Eq. (1) depends on two dimensionless parameters $\eta \in [0, 1]$ and $\chi \in [-\sqrt{7}/2, \sqrt{7}/2]$, that drive the system in between four dynamical-symmetry limits: U(5) for $(\eta, \chi) = (1, 0)$, O(6) for $(\eta, \chi) = (0, 0)$, SU(3) for $(\eta, \chi) = (0, -\sqrt{7}/2)$, and $\overline{\mathrm{SU(3)}}$ for $(\eta, \chi) = (0, \sqrt{7}/2)$; the dynamical symmetry $\overline{\mathrm{O(6)}}$ is not present in the parameter plane (so-called extended Casten triangle [32]).

The classical limit can be constructed by the method of Hatch and Levit [33] using Glauber coherent states. We have outlined the procedure in Ref. [18], where the special case $\chi = 0$ was studied for zero eigenvalue $l(l+1)$ of $L^2$, with the angular momentum defined as $L = \sqrt{10}[d^\dagger\tilde{d}]^{(1)}$. For general $\chi$ and $l = 0$ the Hamiltonian—with the quadrupole deformation parameters $\beta, \gamma$ and their conjugate momenta $p_\beta$, $p_\gamma$ as canonical coordinates—becomes

$$\begin{aligned} H_{\mathrm{cl}} = {} & \frac{1}{2}[\eta + 2(1-\eta)\beta^2](\beta^2 + T) - 2(1-\eta)\beta^2 \\ & - \frac{2}{\sqrt{7}}\chi(1-\eta)\sqrt{1 - \frac{1}{2}(\beta^2 + T)} \\ & \times\left[\left(p_\gamma^2/\beta - \beta p_\beta^2 - \beta^3\right)\cos 3\gamma + 2p_\beta p_\gamma \sin 3\gamma\right] \\ & - \frac{4}{7}\chi^2(1-\eta)\left[\frac{1}{8}(\beta^2 + T)^2 - \frac{1}{2}p_\gamma^2\right]. \end{aligned} \tag{2}$$

Here, $T \equiv p_\beta^2 + p_\gamma^2/\beta^2$ stands for the usual kinetic energy. The Hamiltonian (2) represents the "energy per boson". Coordinates and momenta are limited to intervals $\beta \in [0, \sqrt{2}]$, $p_\beta \in [0, \sqrt{2}]$, and $p_\gamma \in [0, 1]$ following from the boundedness of Hamiltonian (1). Note that classical energy from Eq. (2) is expressed in units of the numerical scaling parameter $a$, see Eq. (1). To distinguish energies obtained from Eqs. (1) and (2), we use hereafter symbols $E$ and $E_{\mathrm{cl}}$, respectively.

In Sec. VII, the classical IBM dynamics will be compared with the dynamics of truncated geometric collective model with Hamiltonian [28–30,34]

$$H_{\mathrm{GCM}} = \frac{1}{2K}T + \underbrace{A\beta^2 + B\beta^3\cos 3\gamma + C\beta^4}_{V_{\mathrm{GCM}}}. \tag{3}$$

In contrast to GCM, the classical IBM Hamiltonian (2) is apparently not a sum of $T$ and a potential $V$. The IBM potential

$$\begin{aligned} V(\beta, \gamma) = {} & \frac{1}{2}(5\eta - 4)\beta^2 + (1-\eta)\left(1 - \frac{1}{14}\chi^2\right)\beta^4 \\ & - \frac{2}{\sqrt{7}}\chi(1-\eta)\beta^3\sqrt{1 - \frac{1}{2}\beta^2}\,\cos 3\gamma, \end{aligned} \tag{4}$$

obtained by setting $p_\beta = p_\gamma = 0$ in Eq. (2), differs from $V_{\mathrm{GCM}}$ in Eq. (3) by the square-root factor. Variables $\beta$ and $\gamma$ can be treated as polar coordinates of the corresponding Cartesian variables $x$ and $y$, thus

$$\begin{aligned} x &= \beta\cos\gamma, & p_x &= p_\beta\cos\gamma - (p_\gamma/\beta)\sin\gamma, \\ y &= \beta\sin\gamma, & p_y &= (p_\gamma/\beta)\cos\gamma + p_\beta\sin\gamma, \end{aligned} \tag{5}$$

with $p_x$ and $p_y$ denoting the associated momenta. This notation will be frequently used below.

Low-energy motions generated by potential (4) undergo essential changes when the first-order shape-phase separatrices are crossed [2–4]. These are located at $\chi = 0, \eta < 0.8$ (prolate-oblate ground-state transition) and $\eta = (4 + 2\chi^2/7)/(5 + 2\chi^2/7) \equiv \eta_{\mathrm{c}}$ (deformed-spherical transition). In panel (b) of Fig. 1 we show a contour plot of the potential for $\eta = 0.5$, $\chi = -0.91$ in the plane $x \times y$, while panel (a) presents three sections in the plane $y = 0$ for the dynamical-symmetry limits. It is worth noting that the value of potential at $\beta = 0$ is always zero; for $\eta < 0.8$ it represents a local maximum while for $\eta > 0.8$ it is a minimum (which becomes global after $\eta_{\mathrm{c}}$).

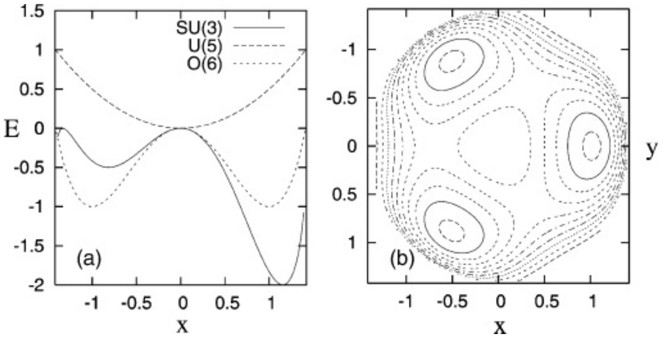

FIG. 1. Sections of potential (4) in the plane $y = 0$ for control parameters corresponding to dynamical symmetries (panel a) and a contourplot of the potential for $\eta = 0.5$ and $\chi = -0.91$ (panel b). Bohr coordinates $\beta$ and $\gamma$ are the radius and polar angle, respectively, in the plane $x \times y$. Energy unit is arbitrary.

## III. ALHASSID-WHELAN SEMIREGULAR ARC

### A. Linear fit of the arc

Location of the highly regular region inside the Casten triangle was determined in Ref. [9] by fitting the minimum of the fraction of chaotic classical phase space volume by a linear dependence. The other classical and quantum measures of chaos (average maximum Lyapunov exponents, spectral correlations, $E2$ strength distributions) showed very similar dependence. The linear fit can be approximated by [26]

$$\chi_{\rm reg}(\eta) \approx \pm\left[\frac{\sqrt{7}-1}{2}\,\eta - \frac{\sqrt{7}}{2}\right]. \tag{6}$$

Note that the arc occurs symmetrically in both $\chi < 0$ and $\chi > 0$ halves of the extended Casten triangle (since the halves are dynamically equivalent, connected by a simple phase transformation). In the following, we will mostly use the convention with $\chi \leqslant 0$.

### B. Classical measures of regularity

While the results of Refs. [5–9] comprehensively reflect the overall dependence of chaotic measures on the model control parameters $\eta$ and $\chi$, some peculiar features of motions related to the increase of regularity remain unaddressed. The present paper offers a closer view on the classical and quantum dynamics at zero angular momentum in the vicinity of the AW arc. In the classical part, the limitation to $l = 0$ admits us to use methods based on Poincaré sections [19] (since the system becomes effectively two-dimensional), which provide neat overall "snapshots" of the phase space at given energy $E$ and allow us to consider stability properties of individual types of trajectories in a simple way. Let us note that Poincaré sections associated with Hamiltonian (1) at lower energies were for the first time studied in Ref. [10]. Here, we extend the study also to higher energies. Several examples of Poincaré sections at $E_{\rm cl} = 0$ can be seen in Fig. 2, where a line crossing the AW arc is followed at a fixed value of parameter $\eta$. The numerical procedure is described in Sec. V A.

To quantify the degree of regularity of a given Poincaré section, we determine the areal fraction $f^{(\rm P)}_{\rm reg}$ occupied by regular trajectories as described in Refs. [28,30]. This method, instead of evaluating the maximal Lyapounov exponent [6,9] associated with each orbit, makes use of the fact that regular orbits fill one-dimensional subsets of the section (topological circles), whereas chaotic orbits fill the available phase space ergodically [19]. The regular fraction is given as the ratio of the area $S_{\rm reg}$ filled with regular trajectories to the total area $S_{\rm tot}$ of the accessible phase space section,

$$f^{(\rm P)}_{\rm reg} = S_{\rm reg}/S_{\rm tot}. \tag{7}$$

A different and faster method we use to determine regularity of the system is based on calculation of the so-called smaller alignment index (SALI) [31] for individual trajectories, randomly generated inside the whole accessible phase space. The regularity is now given as the ratio of the number of regular trajectories $N_{\rm reg}$ to the total number $N_{\rm tot}$ generated at a given values of control parameters and energy, hence

$$f^{(\rm S)}_{\rm reg} = N_{\rm reg}/N_{\rm tot}. \tag{8}$$

Both measures attain values $f_{\rm reg} \in [0, 1]$ and provide an independent verification of increased regularity in the AW arc.

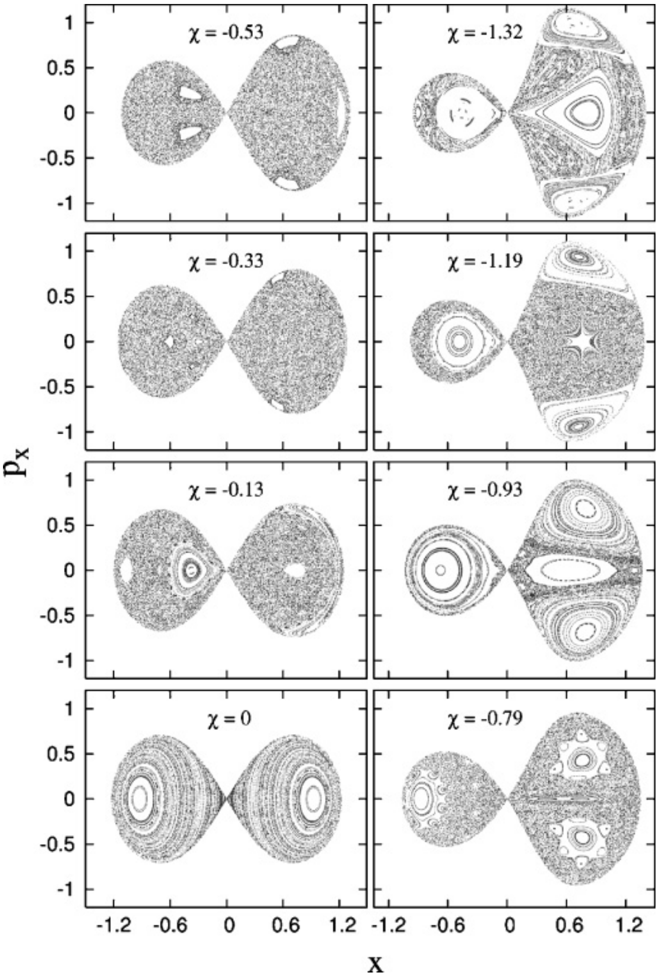

FIG. 2. Phase space portraits disclosed by $E_{\rm cl} = 0$ Poincaré sections at $\eta = 0.5$ and $\chi \in [0, -\sqrt{7}/2]$. Each panel contains $\sim 10^4$ passages of 120 trajectories with $E_{\rm cl} = l = 0$ and randomly generated initial condition through the plane defined by setting $y = 0$. The crossing of the AW arc can be noticed at $\chi \approx -0.9$.

In Fig. 3, we present the dependence of regularity on $\chi$ at $\eta = 0.5$ and $E_{\rm cl} = 0$: both regular fractions decrease monotonously from $f_{\rm reg} = 1$ in the integrable regime $\chi = 0$ to values $f_{\rm reg} < 0.05$ for $\chi \approx -0.4$. Then they rise again to reach $f_{\rm reg} = 0.8$ at $\chi = -0.91$. Decreasing $\chi$ further, the fractions drop to $f_{\rm reg} \approx 0.3$ with a slight increase at $\chi = -\sqrt{7}/2$. In the more efficient SALI calculation, we chose a finer step in $\chi$, which discloses some minor peaks in the interval $\chi \in [-0.8, -0.4]$. In the region of $\eta \approx 0.5$, these are however negligible in comparison with the main regularity increase around $\chi \approx -0.9$.

Poincaré sections in Fig. 2 corresponding to selected values of $\chi$ along the same line show, that in the most chaotic regions, $\chi \in [-0.8, -0.1]$, the phase space consists of a complicated pattern of minor regular regions emerging from

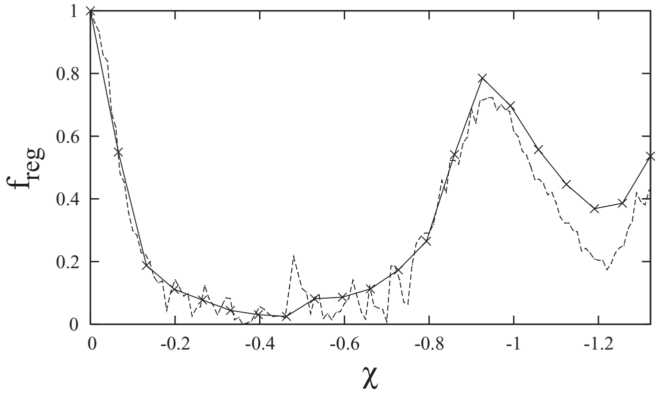

FIG. 3. Regularity of classical IBM for $\eta = 0.5$ and $E_{\rm cl} = 0$ as a function of $\chi$ determined by two methods: (i) the fraction of regular area in the Poincaré section (solid line) and (ii) the fraction of regular trajectories obtained by the SALI method (dashed line). The peak at $\chi \approx -0.9$ corresponds to AW arc. Oscillations on the dashed curve are caused by a finer step of the SALI evaluation.

the "background" of ergodic trajectories. On the other hand, the peak of regularity at $\chi \approx -0.9$ gives rise to a remarkably simple picture containing basically only four major regular islands. These correspond to two families of regular orbits, discussed further in Sec. V.

The degree of regularity is not uniform in energy and the relative regularity of the arc is most significant just around absolute energy $E_{\rm cl} = 0$. This is illustrated in Fig. 4, where we plot the regular fraction (8) for $\eta = 0.5$ and several values of $\chi$ as a function of energy. Our observations conform with the earlier results of Refs. [6–9]. The energy dependence will be studied in more detail in Sec. V.

### C. Quantum measures of regularity

To check the signatures of classical regularity in the quantum spectrum, we fitted the Brody distribution of normalized spacings $S = (E_{i+1} - E_i)/\langle E_{i+1} - E_i\rangle$ between neighboring eigenvalues in the unfolded spectrum of $0^+$ levels. The Brody distribution has the form [35]

$$\mathcal{P}_\omega(S) = \mathcal{N}_\omega S^\omega \exp(-\alpha_\omega S^{1+\omega}) , \tag{9}$$

where $\omega$ is an adjustable parameter, $\alpha_\omega = \Gamma(\frac{2+\omega}{1+\omega})^{1+\omega}$, and $\mathcal{N}_\omega = (\omega + 1)\alpha_\omega$. It interpolates between Poisson distribution ($\omega = 0$) valid for generic integrable systems and Wigner distribution ($\omega = 1$) corresponding to chaotic systems [20,21]. The spectrum was obtained by numerical diagonalisation of Hamiltonian (1) and the subsequent unfolding was performed by methods described in Ref. [36].

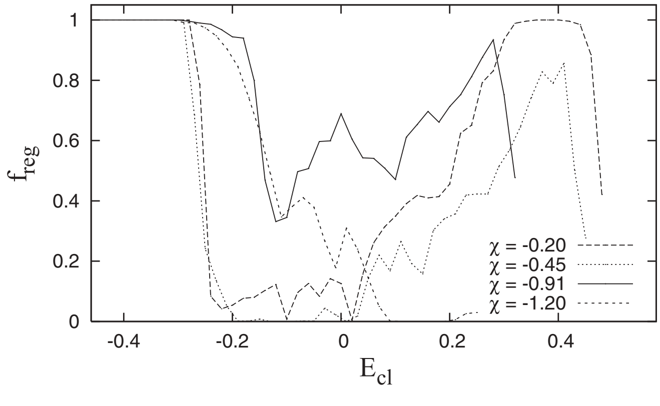

FIG. 4. Energy dependences of regularity in classical IBM for $\eta = 0.5$ at selected values of $\chi$ determined by the SALI method. Energy unit is arbitrary.

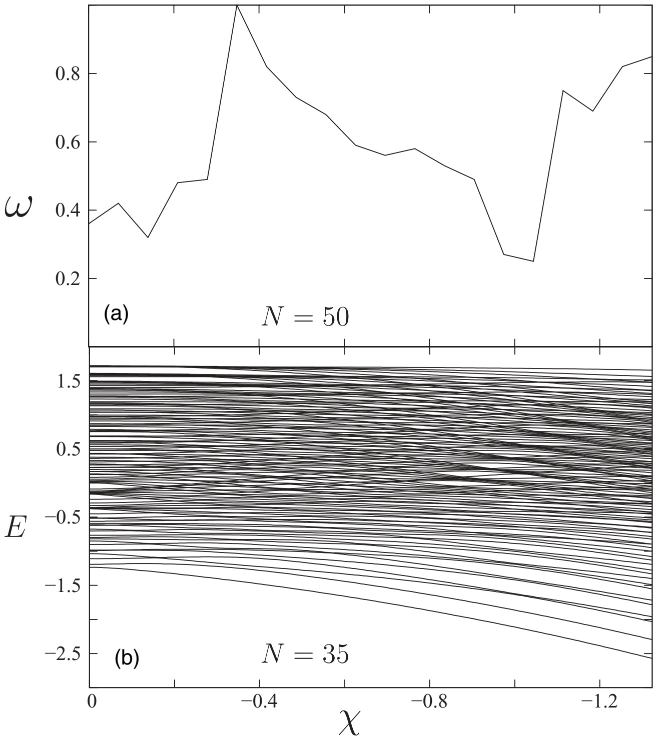

FIG. 5. The evolution of $0^+$ energy levels (panel b) and the corresponding dependence of the Brody parameter $\omega$ on $\chi$ at $\eta = 0.5$ (panel a). The minimum of $\omega$ at $\chi \approx -1$ is connected with the bunching of $E \in [0, 1]$ levels. Energy unit is arbitrary. The boson numbers in each panel differ only to make panel (b) more legible.

In Fig. 5 we show values of the Brody parameter $\omega$ (panel a) and the evolution of $0^+$ energies (panel b) as $\chi$ is varied at $\eta = 0.5$. The dependence of $\omega(\chi)$ has again a clear minimum $\omega \approx 0.25$ corresponding to a Poisson-like distribution (hence quasiregular dynamics) at $\chi \approx -1$. Note that the nonzero value of $\omega$ in the integrable region $\chi = 0$ results from nongeneric spectral fluctuations [9].

We can conclude that both classical and quantum measures $f_{\rm reg}$ and $\omega$ show significant increase of regularity for values close to curve Eq. (6) that predicts $\chi_{\rm reg} \approx 0.91$ for $\eta = 0.5$. However, it should be stressed again that the picture depends very much on energy. Although the increase of regularity can be clearly observed in energy-averaged measures [8,9], the greatest contribution comes from the region around $E \approx 0$ (cf. Fig. 2 of Ref. [8]). If repeating the above classical analysis for another energy value, the AW arc might remain unnoticed.

## IV. BUNCHING OF $0^+$ STATES

In this section, we study the evolution of energy spectra of Hamiltonian (1) with variable $\eta$, following the path along the AW arc. We try to trace out a pattern of multiple bunchings and antibunchings of levels, noticeable already in Fig. 5(b) at $\chi \approx -0.9$, and discuss its relation to a similar structure in the O(6)-U(5) transition [17,18]. We claim that this pattern, for the first time noticed in the analysis of unfolded spectra in Ref. [4] and also reported in Ref. [37], constitutes the most distinctive characteristic of the AW arc.

The pattern can be clearly observed when looking at $\eta$-dependent spectral evolution along the path $\chi_{\rm reg}(\eta)$, Eq. (6). The relevant part of the $0^+$ spectrum for $N = 40$ bosons is plotted in the middle panel [$k = 3$, see Eq. (10) below] of Fig. 6. Note that in this subsection we use a numerical scaling factor $a = N/10$ of quantum Hamiltonian (1), i.e., $a = 4$ energy units for $N = 40$. As seen, the bunching pattern resides slightly above $E = 0$; it starts at $\eta \approx 0.1$, $E \in [0.2, 0.6]$ and spans roughly the whole region of deformed ground-state shapes until it runs off the spectrum at $\eta \approx 0.8$, $E \in [-0.2, 0.2]$.

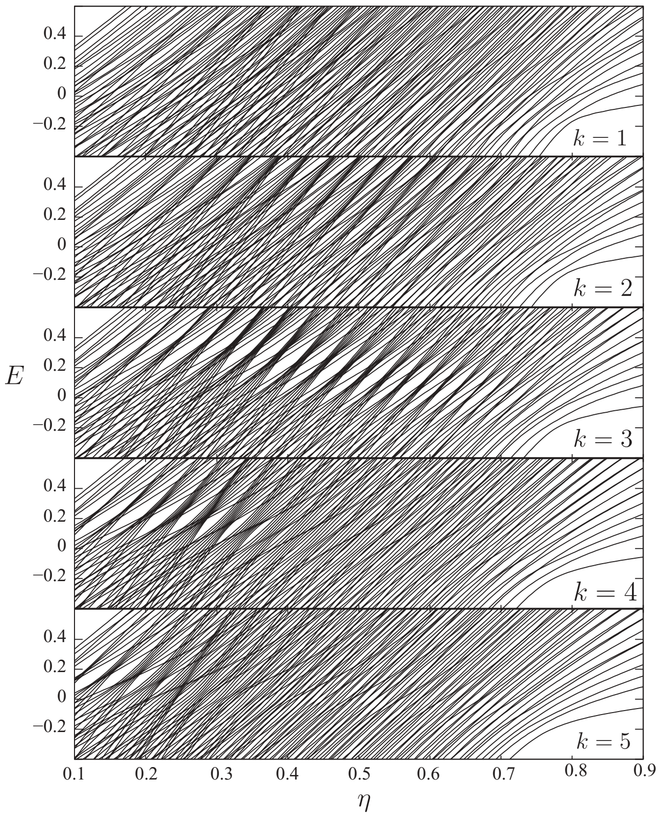

FIG. 6. Evolutions of $0^+$ spectra for $N = 40$ [Hamiltonian (1) with $a = 4$] along paths shown in Fig. 7. Energy unit is arbitrary. A bunching pattern slightly above $E = 0$ is observed in the AW arc (panel $k = 3$) and gradually disappears as the path deviates from the arc (panels with $k \neq 3$).

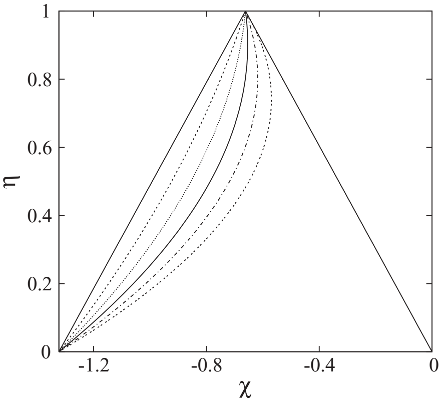

FIG. 7. A set of paths (10) "parallel" to the AW arc (6). The paths are labeled by $k = 0, 1, \ldots, 5$, with $k = 0$ corresponding to the SU(3)-U(5) edge and $k = 3$ representing the arc (solid curve). Only the $\chi \leqslant 0$ half of the extended Casten triangle is shown.

The question arises whether such bunchings may be observed also in neighboring parameter regions. To find the answer, we chose several paths "parallel" with the AW arc, see Fig. 7, and look at the associated spectra in various panels of Fig. 6. The paths are labeled by integer $k$ in the following parametrization:

$$\chi_k = \pm\left[k\frac{\sqrt{7}-1}{6}\eta - \frac{\sqrt{7}}{2}\right], \qquad (10)$$

where $k = 0$ corresponds to the SU(3)-U(5) [or $\overline{\rm SU(3)} - {\rm U(5)}$] edge of the Casten triangle while $k = 3$ to the fit (6) of the arc. Apparently, the bunching fades away as we depart from the arc. Since, as mentioned in Sec. III, the regularity within the AW arc for low spins is mostly connected with the region around and just above zero absolute energy (cf. Fig. 4 above and Fig. 2 of Ref. [8]), we anticipate that the bunching (present in the same range) is intimately related to the source of regularity.

Another immediate question is whether the bunching survives an increase of angular momentum. Figure 8 shows that when increasing the angular momentum eigenvalue $l$, the gaps in the spectrum become less pronounced due to repulsion among increased numbers of levels. For low spins a tendency to bunch is still observable in the same range of energies, but the effect is practically gone for $l \geqslant 8$.

Figure 9 offers a comparison of the bunching pattern in the AW arc (lower panel) with a similar pattern along the integrable O(6)-U(5) transition [17,18,38] (upper panel). It is clear that both structures exist at $l = 0$ in very close (although not identical) energy domains, $E \approx 0$, and exhibit great deal of similarity. On the other hand, while in the O(6)-U(5) transition the bunching involves real crossings of levels with different seniority quantum numbers, all crossings along the AW arc are presumably avoided (though to prove this numerically is, in some cases, practically impossible). It can be noticed that if proceeding along the bunching from the right ($\eta \approx 0.8$) to the left, the numbers of states involved form a sequence 1, 2, 3, 4, 5, . . ., in the O(6)-U(5) case and 1, 1, 2, 2, 3, 3, . . ., in the AW case.

With increasing $\eta$, the center of the bunching in both O(6)-U(5) and AW cases travels toward the kink of the ground-state energy at $\eta = \eta_c$ which separates the deformed and spherical phases [2–4]. As shown recently [38], the $E = 0$ bunching along the O(6)-U(5) path demarcates the $N \to \infty$

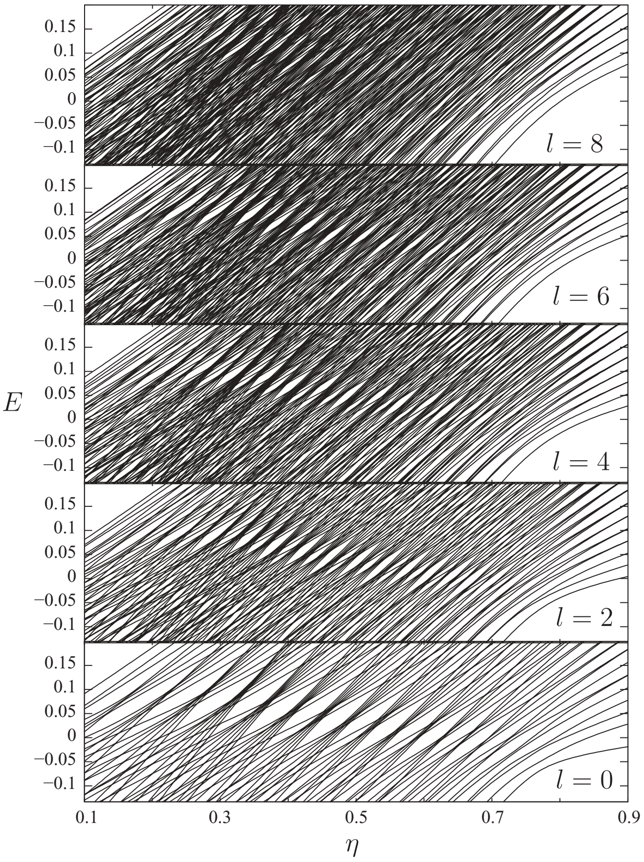

FIG. 8. Washing out of the bunching pattern at $\chi_{\text{reg}}(\eta)$ ($k = 3$) with increasing angular momentum $l$ for $N = 30$. (Energy unit is arbitrary.)

phase transition of excited states with zero seniority. It would be interesting to learn whether the pattern in the AW arc has a similar consequence (although seniority is not defined in this case).

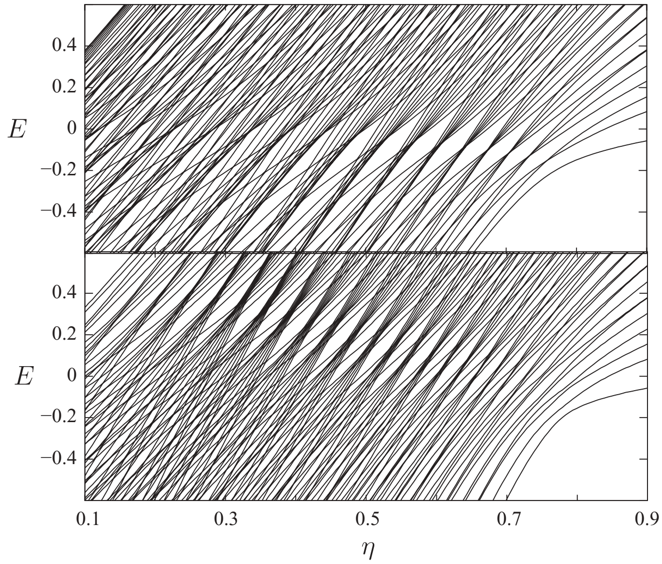

FIG. 9. Comparison of the bunching of $0^+$ states in O(6)-U(5) transition (upper panel) and along the AW arc (lower panel); both spectra calculated for $N = 40$. (Energy unit is arbitrary.)

## V. CLASSICAL EFFECTS

### A. Numerical procedure

In the following, we discuss classical phase-space structures arising from Hamiltonian (2) that uncover various types of regular motions in different parts of the Casten triangle. We focus in particular on classical motions within the AW arc.

To make a detailed image of the IBM phase space, a sufficient number of trajectories must be launched, covering the whole plane of the Poincaré section, and each of them must be traced for sufficiently long time. In our calculations, we generated 120 trajectories with random initial conditions (satisfying the constraint $l = 0$) for every set of $\eta$, $\chi$, and $E_{\text{cl}}$. The classical equations of motions corresponding to Hamiltonian (2) were solved numerically, using the fourth-order Runge-Kutta method, and the calculation was stopped after $3 \times 10^4$ passages of each trajectory through the $x \times p_x$ plane with $y = 0$.

The method of evaluating the areal fraction $f_{\text{reg}}^{(\text{P})}$ from Eq. (7) was described in Ref. [30]. Finite resolution of the Poincaré section division leads to some systematic errors which are most significant when $f_{\text{reg}}^{(\text{P})} \approx 1$ but do not exceed cca 5%. The implementation of the SALI method (for details, see Ref. [31]) in the evaluation of $f_{\text{reg}}^{(\text{S})}$ from Eq. (8) induces statistical errors connected with the finite numbers of generated trajectories. In our case ($N_{\text{tot}} = 500$ for each point of $f_{\text{reg}}^{(\text{S})}$) the error is estimated by the expression $\Delta f_{\text{reg}}/f_{\text{reg}} \approx 0.04 f_{\text{reg}}^{-1/2}$.

The energy dependence of the degree of chaos at selected values of $\eta$ and $\chi$ is explored with a sample of ten equidistant levels

$$E_i = V_{\text{min}} + \frac{i}{11}\left(V_{\text{lim}} - V_{\text{min}}\right), \tag{11}$$

$i = 1, \ldots, 10$, covering the whole energy range between the global minimum $V_{\text{min}} = V(\beta = \beta_{\text{min}})$ of the potential for given $\eta$, $\chi$ and the value $V_{\text{lim}} \equiv V(\beta = \sqrt{2})$, which represents the uppermost energy for the classical motion to be finite (since $\beta = \sqrt{2}$ is the maximal physical value of the deformation parameter). Remind that energies $E_{\text{cl}}$ obtained from classical Hamiltonian (2) are scale-free, i.e., given in units of $a$ (in contrast to quantum energies $E$ analyzed in Sec. IV). We point out two important intermediate energy values: (i) Energy $E_{\text{sad}} < 0$ of the saddle points between three degenerate global $\beta > 0$ minima of potential (4) at $\gamma = 0, 2\pi/3$, and $4\pi/3$. Below $E_{\text{sad}}$, the energetically accessible region in the plane $x \times y$ consists of three separate areas surrounding the global minima; at $E_{\text{cl}} = E_{\text{sad}}$ these areas touch and merge. (ii) The energy $E_{\text{cl}} = 0$ coinciding with the local maximum $V(\beta = 0)$. For $E_{\text{cl}} > 0$ the accessible region in the $x \times y$ plane is a simply connected area.

### B. Poincaré sections

Poincaré sections corresponding to $E_{\text{cl}} = E_1, \ldots, E_{10}$ from Eq. (11) were generated at 35 points lying on paths $\chi_k$, Eq. (10), with $k = 0, 1, \ldots, 5, 7$ and $\eta \in [0.3, 0.7]$. The results show a sensitive dependence of the dynamics on $\chi$, with particularly distinct structural changes of trajectories in the vicinity of the AW arc ($k = 3$), for all values of $\eta$. On the other hand, varying $\eta$ for a fixed $k$ affects the motions mostly via shifting both energy limits $V_{\rm min}$ and $V_{\rm lim}$ upward (thus energies $E_{\rm cl} < 0$ become unattainable for $\eta > \eta_{\rm c} \approx 0.8$), but the shape of the main phase space structures far enough from $\eta_{\rm c}$ remains visually intact.

A complete collection of Poincaré sections may be found on our website [39]. Here we will illustrate the dependence of the dynamics on $\chi$ at $\eta = 0.5$, by selecting three values $\chi_k$ with $k = 2, 3, 4$, that represent the regions of $|\chi| > |\chi_{\rm reg}|$, $\chi = \chi_{\rm reg}$, and $|\chi| < |\chi_{\rm reg}|$, respectively. The corresponding Poincaré sections are arranged in three columns of Fig. 10. Rows from bottom to top correspond to increasing energies from Eq. (11). Note that values of $E_i$ differ for the three columns (because the shape of potential depends on $\eta$ and $\chi$), but energy ranges below and above the above-specified benchmarks $E_{\rm cl} = 0$ and $E_{\rm sad}$ can be easily recognized from the topology of the respective section: While for $E_{\rm cl} < E_{\rm sad}$ (no pass between three degenerate global minima) the crossings form a single compact area around $x \approx \beta_{\rm min} > 0$, $p_x = 0$, for $E_{\rm cl} > E_{\rm sad}$ we observe two separate areas of crossings (with $x > 0$ and $x < 0$) that merge at $E_{\rm cl} = 0$. For $E_{\rm cl} > 0$, the crossings fill in a single area around the origin.

Regular trajectories contributing to Poincaré sections in Fig. 10 form islands of concentric "circles" enfolding some simple periodic orbits in their centers. Examples are given in Fig. 11. The central orbits represent *elliptic* fixed points of the associated Poincaré mapping [19] and can be used to classify the enveloping islands. We distinguish the following principal families of orbits:

(i) Trajectories forming a regular island centered at a point $x > 0$ and $p_x = 0$. These constitute a family of "$\gamma$-vibrations" since the central orbit (see orbit 1 in both panels of Fig. 11) oscillates with $\beta \approx \beta_{\rm min}$ around the potential minimum. (To avoid confusion we note that in the present case angular momentum $l = 0$, which is in contrast to the lowest $\gamma$-vibrational quantum state with $l = 2$.)

(ii) Trajectories forming two symmetric regular islands with central points at $x > 0$ and $p_x > 0$, $p_x < 0$ and for $E_{\rm cl} > E_{\rm sad}$ also an additional island at $x < 0$ and $p_x = 0$. These are mixed "$\beta\gamma$-vibrations" that for $E_{\rm cl} < E_{\rm sad}$ oscillate around one potential minimum [see both orbits 2 in panel (a) of Fig. 11] and for $E_{\rm cl} > E_{\rm sad}$ migrate over the saddle points between the pairs of neighboring minima [orbits $2_{\rm a}$ and $2_{\rm b}$ in panel (b) of Fig. 11 connecting the $\gamma = 2\pi/3$ and $4\pi/3$ minima; analogous orbits exist also for the other pairs of minima].

We observe (cf. Figs. 4 and 10) that the degree of chaos varies with $\chi$ most significantly at intermediate energies, especially around $E_{\rm cl} \approx 0$ (cf. Sec. IV). At low energies, $E_{\rm cl} < E_{\rm sad}$, but also at very high energies, $E_{\rm cl} \approx V_{\rm lim}$, the dynamics is mostly regular—this being understood from the prevailing harmonic and pure quartic character of collective oscillations in the respective regimes [30]. In the following,

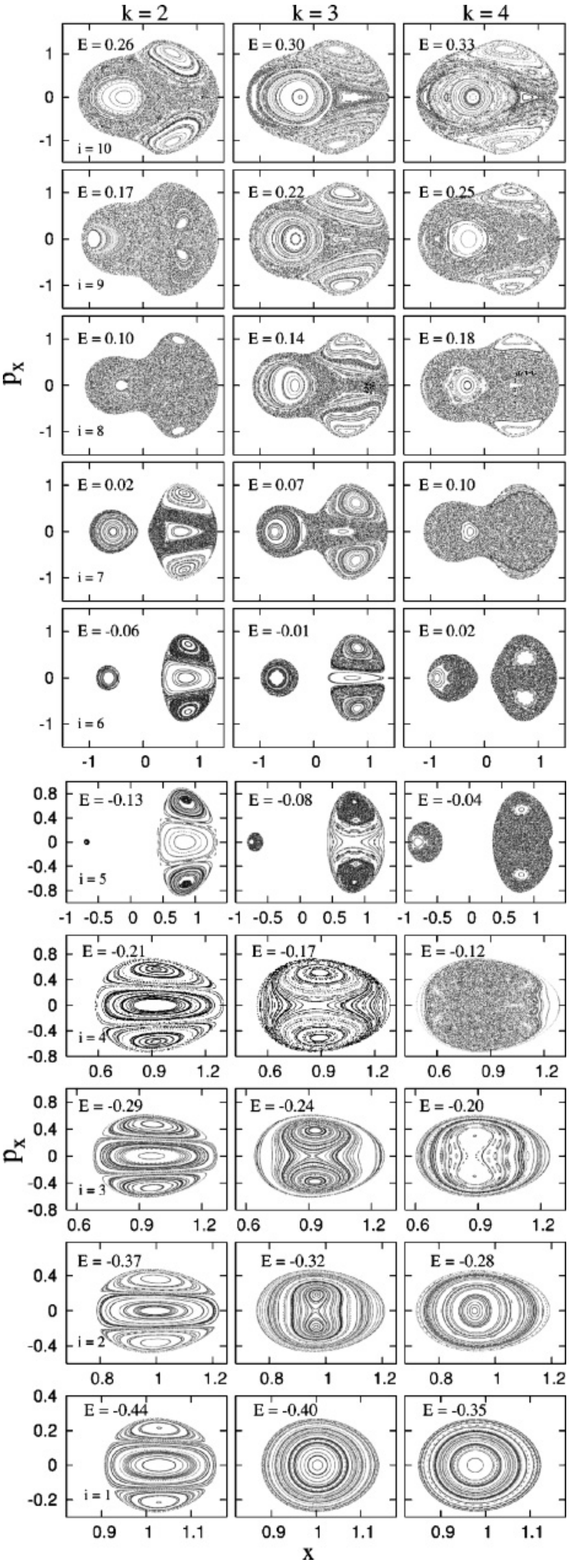

FIG. 10. Poincaré sections $y = 0$ for $\eta = 0.5$ and $\chi_k$, $k = 2, 3, 4$ (columns) at energies $E_{\rm cl} = E_1, \ldots, E_{10}$ (rows). The middle column corresponds to the AW arc. Notice that sections for $E_{\rm cl} < E_{\rm sad}$ are expanded compared to those for $E_{\rm cl} \geqslant E_{\rm sad}$.

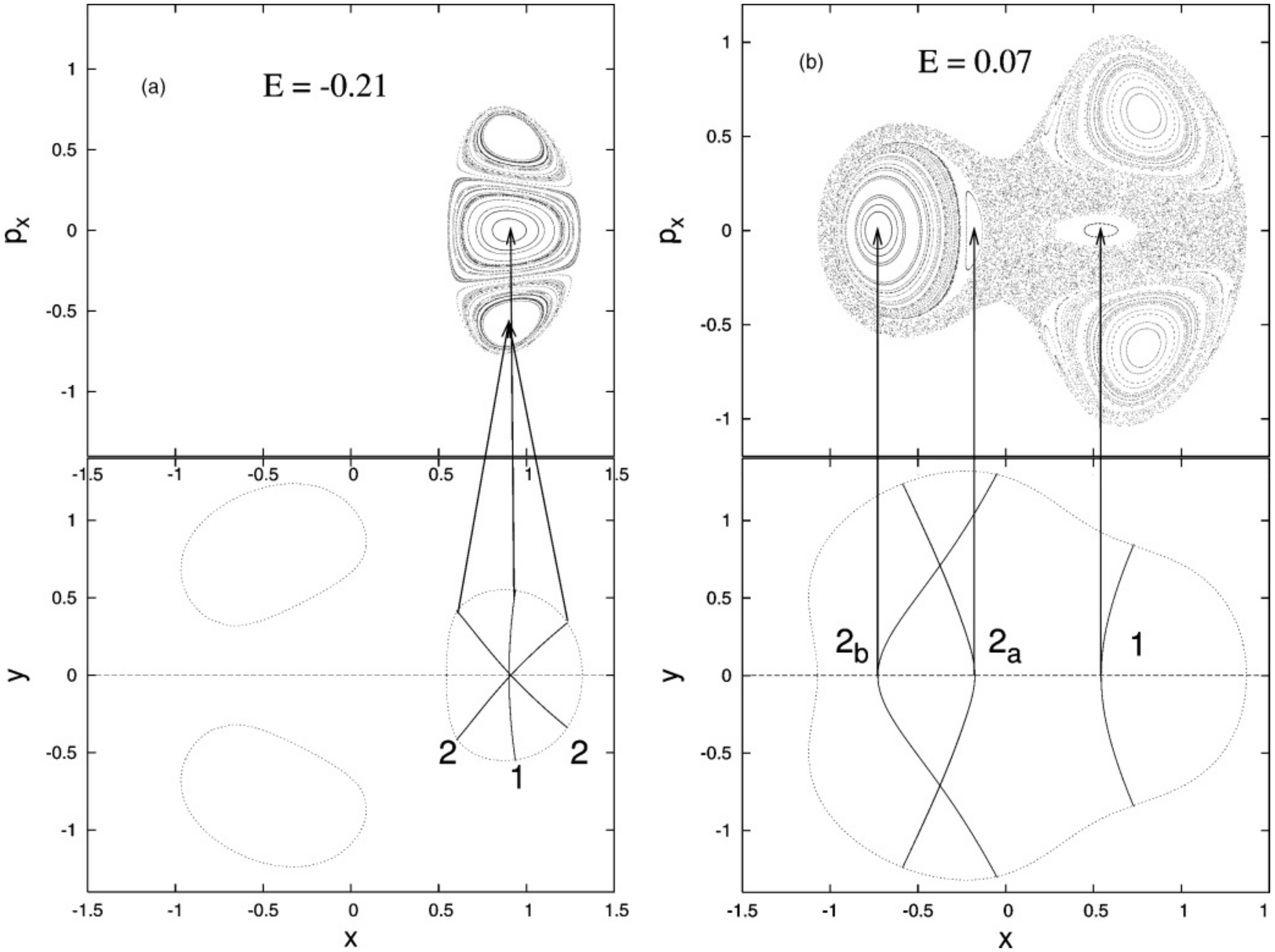

FIG. 11. Poincaré sections and the central periodic orbits corresponding to the principal regular islands in the vicinity of the AW arc. In both panels $\eta = 0.5$. Panel (a) corresponds to $E_{\rm cl} = E_4 < E_{\rm sad}$, $\chi = \chi_2$, panel (b) to $E_{\rm cl} = E_7 > 0$, $\chi = \chi_3$ (cf. the respective sections of Fig. 10). The dashed lines at $y = 0$ demarcate the plane of section and the arrows show the position of individual orbits in the Poincaré sections.

we describe features of motions characteristic for the three regions with respect to the regular arc.

$|\chi| > |\chi_{\rm reg}|$ ($k = 2$ column of Fig. 10): The low-energy behavior below $E_{\rm sad}$ ($E_1, \ldots, E_4$) is completely regular, dominated by $\gamma$ and $\beta\gamma$ vibrations (types 1 and 2). The Poincaré section at $E_5$ reflects merging of the hitherto separate accessible regions. The rims of the regular islands get chaotic around $E_6$, $E_7$. Increasing the energy further, chaos prevails destroying the regular family around the type 1 and only tiny regular areas roughly in the previous position of the three regular islands of type 2 are left. At the highest energies, around $E_{10}$, the regular islands of the type-2 vibrations spread significantly, increasing $f_{\rm reg}$ to $\approx 0.5$.

$\chi = \chi_{\rm reg}$ ($k = 3$ column of Fig. 10): The single island of type-1 $\gamma$-vibrations present at the lowest energies ($E_1$) splits in its center into two smaller islands corresponding to vibrations of type 2 (see panels $E_2, \ldots, E_5$). Unlike in the previous case, the $\gamma$-vibration now constitutes a *hyperbolic* fixed point [19]. Interestingly, it becomes elliptic again around $E_{\rm cl} \approx 0$ [(see regular islands around $x > 0$, $p_x = 0$ in panels $E_6$ and $E_7$ of Fig. 10 and panel (b) of Fig. 11] and subsequently “disappears” in a sea of chaos at $E_8$. Another distinctive fact is a *crossover* of the $2_{\rm a}$ and $2_{\rm b}$ types of $\beta\gamma$-vibrations slightly above $E_{\rm cl} = 0$ (see $E_7$): one of the outermost tori of mixed vibrations (with central orbit of type $2_{\rm b}$) disintegrates to produce a new island of regular trajectories (type $2_{\rm a}$), which with increasing energy “expels” the original island of type $2_{\rm b}$ orbits toward the boundary of the accessible region. At $E_9$ and $E_{10}$, a new family or regular orbits appears: these circle around the whole accessible region giving rise to two new islands. It is worth noting that the regular islands corresponding to $\beta\gamma$-vibrations (types 2 or $2_{\rm a}$, $2_{\rm b}$) exist in the whole energy range between $E_2$ and $E_{10}$ and that the low-energy form of these trajectories (type 2) reminds strongly the trajectories of the SU(3) limit.

$|\chi| < |\chi_{\rm reg}|$ ($k = 4$ column of Fig. 10): The process starts in a similar way as for $\chi = \chi_{\rm reg}$, with the $\gamma$-vibration becoming hyperbolic around $E_3$, but the enveloping “circles” disintegrate into complicated Poincaré-Birkhoff chains of alternating elliptic and hyperbolic fixed points [19] which usher in strong chaos resident at higher energies, $E_4, \ldots, E_7$.

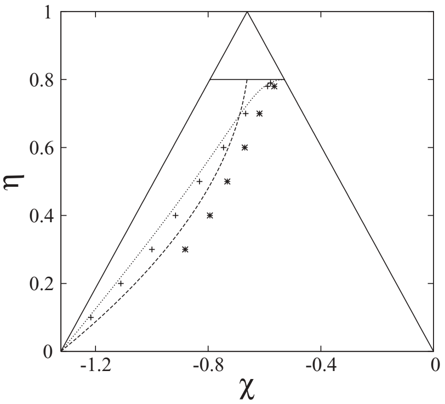

FIG. 12. The AW arc [Eq. (6), the dashed curve] and the locus of degeneracy of $\beta$ and $\gamma$ bandheads [Sec. VI, the dotted curve] inside the Casten triangle. The points mark the change of stability of $\gamma$-vibrations (orbits of type 1 in Fig. 11) at $E_{\mathrm{cl}} = -|V_{\min}|/2$ (crosses) and at $E_{\mathrm{cl}} = 0$ (asterisks), see Subsec. V B. Numerical errorbars are smaller than the pointsize.

At the highest energies the regularity rises again; the Poincaré section at $E_{10}$ yields $f_{\mathrm{reg}} \approx 0.8$.

The scenarios described above hold for the whole region $\eta < 0.6$. As already pointed out in Refs. [10,11], the vicinity of AW arc can be recognized as a place where the $\gamma$-vibrations (type-1 orbits) change their character from elliptic ($|\chi| > |\chi_{\mathrm{reg}}|$) to hyperbolic ($|\chi| < |\chi_{\mathrm{reg}}|$) fixed points. Note that at *low energies* ($E_{\mathrm{cl}} < 0$), the change of stability of the central $\gamma$-vibration is always accompanied by stability changes of the outermost enveloping "circles" in Poincaré sections, which in turn represent almost pure $\beta$-vibrations (for our choice of the phase space section, $y = 0$, these do not represent fixed points). The stability properties of $\beta$-vibrations are opposite to those of $\gamma$-vibrations: they are stable in the region where $\gamma$-vibrations are unstable and vice versa. This happens very close to $\chi_{\mathrm{reg}}$ on the SU(3)-U(5) side of the triangle. On the other hand, at *higher energies* ($E_{\mathrm{cl}} \approx 0$), the $\gamma$-vibrations change stability on the other side of $\chi_{\mathrm{reg}}$. This may be seen in Fig. 12, where the stability changes at $E_{\mathrm{cl}} = -|V_{\min}|/2$ and at $E_{\mathrm{cl}} = 0$ are marked by crosses and asterisks, respectively.

When approaching the phase transition, for $0.6 < \eta < 0.8$, the loci of $E_{\mathrm{cl}} < 0$ and $E_{\mathrm{cl}} \approx 0$ stability changes discussed above deviate from the curve $\chi_{\mathrm{reg}}(\eta)$ from Eq. (6). In fact, the linear fit of the regular arc becomes inaccurate in this region and changes in classical dynamics follow rather the curve $\chi_{\mathrm{deg}}(\eta)$ of the $\beta$- and $\gamma$-bandhead degeneracy (dot-dashed curve in the Fig. 12), which will be discussed further in Sec. VI.

As a final remark we point out that crossing of the SU(3)-U(5) edge of the Casten triangle, in contrast to crossing of the AW arc, does not bring about any significant change in dynamics.

### C. Periodic orbits

In this subsection, we will discuss a possible relation of stability changes in classical dynamics (as described in Sec. V B) to the $E \approx 0$ bunching pattern in quantum spectra (Sec. IV). In particular, we focus on the crossover between the two types of $\beta\gamma$-vibrations (orbits $2_{\mathrm{a}}$ and $2_{\mathrm{b}}$ in Fig. 11) and on the temporal resurrection of $\gamma$-vibrations (orbit 1 therein), both these phenomena taking place in the relevant energy and parameter domains (cf. panels $E_6$ and $E_7$ of Fig. 10).

The influence of classical dynamics on quantized energy spectra is described in the framework of semiclassical periodic orbit theory [19–21]. The oscillating part $\rho_{\mathrm{osc}}(E)$ of the quantum level density can be be expressed via so-called trace formulas, which depend on properties of classical periodic trajectories and have the following generic form:

$$\rho_{\mathrm{osc}}(E) = \frac{1}{\pi\hbar} \sum_{p} \sum_{r=1}^{\infty} \frac{r T_p}{A_p} \cos\left[\frac{r S_p(E)}{\hbar} - r\mu_p \frac{\pi}{2}\right]. \quad (12)$$

The sum is running over all primitive orbits $p$ with period $T_p$ together with their multiple retracings $r = 1, 2, 3, \ldots$. The argument of the cosine is determined by the action

$$S_p(E) = \oint \vec{p} \cdot d\vec{q} = \int_0^{T_p} \vec{p} \cdot \dot{\vec{q}}\, dt \quad (13)$$

along the primitive orbit and the number of caustics $\mu_p$ (Maslow index) encountered there. Inverse amplitude $A_p$ reflects the stability properties of the orbit and depends on the nature of dynamics. The explicit form of $A_p$ is known only for completely regular or chaotic systems, respectively, given by the Berry-Tabor formula for contributions of tori [40] and Gutzwiller formula for contributions of isolated orbits [41].

The level bunching described in Sec. IV constitutes a significant fluctuation in level density. We may therefore expect that it is connected, through Eq. (12), with changes in properties of classical periodic orbits. In Sec. V B, the increased regularity of $l = 0$ motions in the AW arc was shown to be basically due to regular trajectories surrounding the vibrations of types 1 and 2 (see Fig. 11). Although we are not able to perform the semiclassical calculation of the level density for a mixed regular/chaotic system such as the IBM (the formula is not known), we will show that stability intervals of the above types of motions and crossover energies are strongly correlated with the bunching pattern.

For this purpose, we calculated actions (13) of orbits from Fig. 11 using a numerical approximation $S_p = \sum(p_x \Delta x + p_y \Delta y)$ in variables (5), where the sum runs over all calculated points until the orbit closes. The energy dependences of $\cos S_p$ for the three types of orbits are presented in Fig. 13 for $\chi = \chi_{\mathrm{reg}}$ and $\eta = 0.35$ (panel a), $\eta = 0.5$ (panel b), and $\eta = 0.65$ (panel c). Individual curves end at the values of energy, where the respective trajectories turn unstable and the surrounding regular islands disappear. The classical energy $E_{\mathrm{cl}}$ from Hamiltonian (2) is related to quantum energy $E$ scaled by $a = N/10$ via $E = 4E_{\mathrm{cl}}$ (for $N = 40$, see Figs. 6 and 9). The energy interval where the bunching of quantum spectrum resides for the given value of $\eta$ is demarcated by the shaded area in the respective panel of Fig. 13.

As we observe, the upper edge of the energy gap demarcating the bunching pattern coincides almost precisely with the endpoint of $2_{\mathrm{b}}$ orbits, while the crossover energy of $2_{\mathrm{a}}$ and $2_{\mathrm{b}}$ orbits takes place within the gap. This is so for all selected values of $\eta$ (panels a–c of Fig. 13). It also turns out that both orbits $2_{\mathrm{a}}$ and $2_{\mathrm{b}}$ match their periods just above the crossover

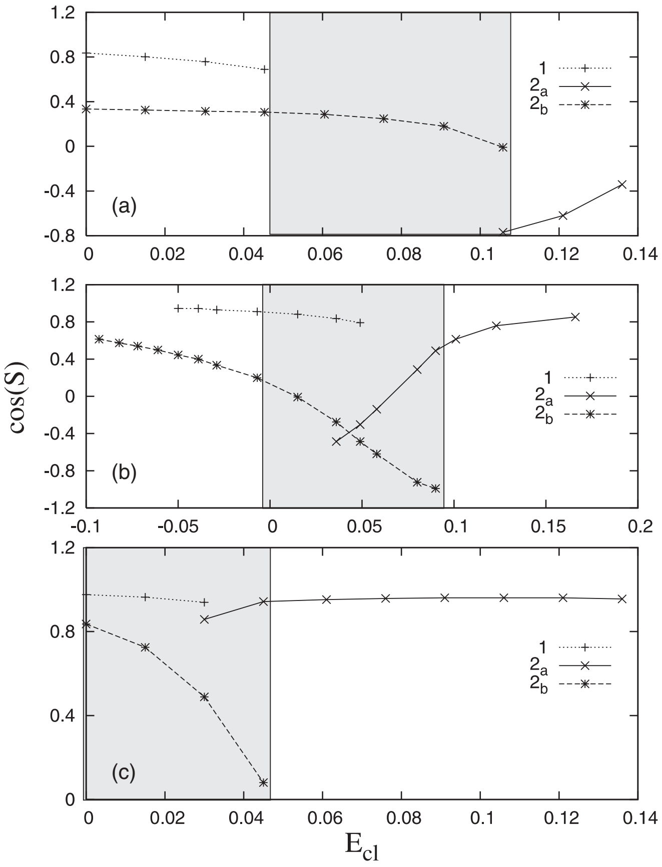

FIG. 13. Oscillating contributions to the state density calculated for the central periodic orbits from Fig. 11 at $\chi = \chi_{\mathrm{reg}}$ and $\eta = 0.35$ (a), 0.5 (b), 0.65 (c). Maslow index $\mu_p = 4$ for all orbits makes no change of the cosine. Grey zones indicate the regions corresponding to the bunching of quantum levels. (Energy unit is arbitrary.)

energy, within the shaded area. The stability changes of type-1 orbits are also correlated with the bunching, although in this case the energy match does not behave in a systematic way.

These findings provide a strong support to the hypothesis that the quantum bunching pattern discussed in Sec. IV is closely connected with the stability changes of the above orbits, in particular with the crossover between $2_a$ and $2_b$ vibrations. Whether this is just an interplay of accidents or a deeper effect resulting from internal symmetries of the system remains an open question.

## VI. $\beta$ AND $\gamma$ BANDHEAD DEGENERACY

In attempts to fit nuclear spectra with the simplified Hamiltonian (1), an approximate degeneracy of $0_2^+$ and $2_2^+$ states (belonging to so-called $\beta$ and $\gamma$ bands, respectively) was found to be a useful tool for identification of nuclei close to the AW arc [27]. Here we estimate the locus of the $0_2^+$-$2_2^+$ degeneracy region in the Casten triangle analytically, by means of the intrinsic-state formalism [42]. It will turn out that the curve $\chi_{\mathrm{deg}}(\eta)$ expressing the locus lies indeed very close to the AW arc $\chi_{\mathrm{reg}}(\eta)$.

In the intrinsic-state formalism, the unprojected wave functions for the ground-state band, $\beta$-band, and $\gamma$-band are up to a combinatorial factor given by

$$\begin{aligned} &|K=0,\mathrm{gs}\rangle \propto \Gamma_0^{\dagger N}|0\rangle\,, \quad |K=0,\beta\rangle \propto \Gamma_\beta^\dagger \Gamma_0^{\dagger N-1}|0\rangle, \\ &|K=2,\gamma\rangle \propto \Gamma_\gamma^\dagger\, \Gamma_0^{\dagger N-1}|0\rangle \end{aligned} \tag{14}$$

with

$$\begin{aligned} &\Gamma_0^\dagger = \frac{1}{\sqrt{1+\beta^2}}[s^\dagger + \beta d_0^\dagger], \quad \Gamma_\beta^\dagger = \frac{1}{\sqrt{1+\beta^2}}[-\beta s^\dagger + d_0^\dagger] \\ &\Gamma_\gamma^\dagger = \frac{1}{\sqrt{2}}[d_2^\dagger + d_{-2}^\dagger]. \end{aligned} \tag{15}$$

The deformation parameter $\beta$ is determined by minimizing the ground state energy

$$E_{\mathrm{g.s.}} = \langle K=0, \mathrm{g.s.}|H|K=0, \mathrm{g.s.}\rangle \tag{16}$$

while the excitation energies of the $\beta$ and $\gamma$ bandheads consequently follow from

$$E_\beta^* = \langle K=0, \beta|H|K=0, \beta\rangle - E_{\mathrm{g.s.}}, \tag{17}$$

$$E_\gamma^* = \langle K=2, \gamma|H|K=2, \gamma\rangle - E_{\mathrm{g.s.}}. \tag{18}$$

The minimization of the ground-state energy (16) and equality of expressions (17) and (18) lead—after taking the $N \to \infty$ limit—to two simultaneous equations in $\eta, \chi$, and $\beta$. Elimination of $\beta$ gives the dependence $\chi_{\mathrm{deg}}(\eta)$, which is shown in Fig. 12 together with the linear fit $\chi_{\mathrm{reg}}(\eta)$ of the AW arc, Eq. (6).

We see in Fig. 12 that both curves $\chi_{\mathrm{deg}}(\eta)$ and $\chi_{\mathrm{reg}}(\eta)$ are relatively close to each other for $\eta < 0.7$. The agreement even slightly improves if we compare $\chi_{\mathrm{deg}}(\eta)$ directly with the points in Fig. 13 of Ref. [9] without the fit (6). As $\eta$ approaches 0.8 both curves diverge. Indeed, since at $\eta = \eta_c \approx 0.8$ the spherical configuration of the ground state is reached, the notion of $\beta$ and $\gamma$ bands looses its sense. Note, however, that the whole spherical region with $\eta > \eta_c$ behaves rather regularly and the concept of the semiregular arc is not well defined here. Notably, both loci of classical-orbit changes discussed in Sec. V apparently follow the $\chi_{\mathrm{deg}}(\eta)$ curve instead of $\chi_{\mathrm{reg}}(\eta)$.

Note that the present procedure equating the bandhead energies of the $\beta$ and $\gamma$ vibrational bands differs somewhat from that of Ref. [27] where energies of the $0_2^+$ and $2_2^+$ states are compared. Namely, the rotational energy shifts up the position of the $2_2^+$ state from the $\gamma$ bandhead energy. For the near rotor nuclei discussed in Ref. [27] this does not make a substantial difference as the rotational energy is small as compared to the excitation energy of the $\gamma$ bandhead. In some cases inspected in Ref. [27], the $2_2^+$ state even belongs to the $\beta$-band, then however $\gamma$-band is still close to the $\beta$-band. For the near vibrator nuclei, the comparison is less straightforward. Here, however, the comment of the previous paragraph applies.

A rotational $L \cdot L$ term can remove the degeneracy of states of different spins but does not change eigenfunctions and the extent of regularity. Then a link of the regular region to the $2_2^+$-$0_2^+$ degeneracy may somewhat be hidden. On the other hand, the $L \cdot L$ term shifts also the relative position of the $\beta$ and $\gamma$ bands. This shift is, however, of the order of $1/N$ as compared to the effect of all other two-body terms of the

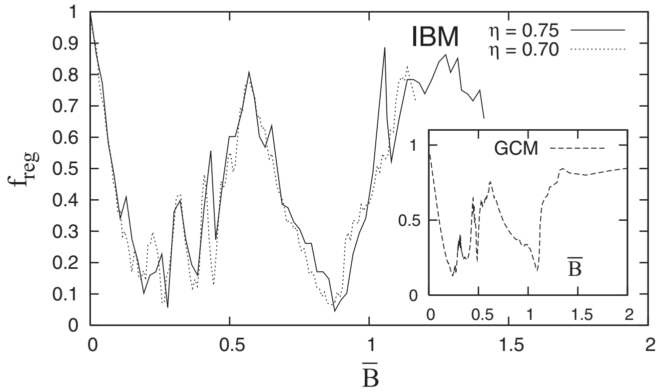

FIG. 14. Regularity $f_{\rm reg}^{(S)}$ at $E_{\rm cl} = 0$ as a function of $\bar{B} = B/\sqrt{|AC|}$ and $\bar{B}(\eta, \chi)$ in the GCM and IBM, respectively, determined by the SALI method.

general IBM Hamiltonian. Of course, the latter deficiency of the $L \cdot L$ term could be balanced by coefficient $\sim N$ of that term. Then the unprojected version of the intrinsic-state formalism ceases to be valid and the angular momentum projection should be considered [43].

## VII. RELATION TO GEOMETRIC MODEL

Recent analyses [28–30] of the classical GCM displayed an unexpectedly complicated dependence of chaoticity on the control parameters and energy. It is certainly interesting to find out whether at least some of the distinctive features of GCM phase space can be "mapped" onto the more realistic IBM. We are going to set focus on the energy $E_{\rm cl} \approx 0$, connected with the most dramatic changes of regularity in the GCM as well as in the IBM case.

We start with an expansion of the square root in the IBM Hamiltonian (2), which up to first order in $(\beta^2 + T)/2$ gives

$$\begin{aligned} H'_{\rm cl} = {} & \frac{1}{2K'}T + A'\beta^2 + B'\beta^3\cos 3\gamma + C'\beta^4 \\ & + \frac{B'}{4}\left(2p_\beta p_\gamma + p_\gamma^2/\beta - \beta p_\beta^2\right)(\beta^2 + T - 4)\sin 3\gamma \\ & - \frac{B'}{4}(\beta^3 T\cos 3\gamma + \beta^5) + D'\beta^2 T + E'\left(\frac{1}{2}p_\gamma^2 - \frac{1}{8}T^2\right) \\ \equiv {} & H'_{\rm GCM} + H'_{\rm res}. \end{aligned} \tag{19}$$

We may immediately identify the GCM-like Hamiltonian (3) in the first line. The residual terms $H'_{\rm res}$ in the next two lines contain a correction $\propto \beta^5$ in the potential and a collection of rather complicated kinetic terms. The coefficients $A', \ldots, E'$ are functions of $\eta, \chi$: $A', B', C'$ being equal to respective factors in Eq. (4), while $K' = 1/\eta$, $D' = (1-\eta)(1-\chi^2/7)$, $E' = 4\chi^2(1-\eta)/7$. The expansion (19) is justified only for small amplitude vibrations around an equilibrium deformation satisfying $\beta_0^2 \ll 1$, which is for $E_{\rm cl} \approx 0$ fulfilled in a region near to the phase transition, $\eta \in [0.7, 0.8]$. It needs to be stressed that even in this region $H'_{\rm res}$ contains kinetic terms of the same order as $T$. One therefore cannot expect a perfect match with the GCM results. Nevertheless, as shown below, the similarity is appreciable.

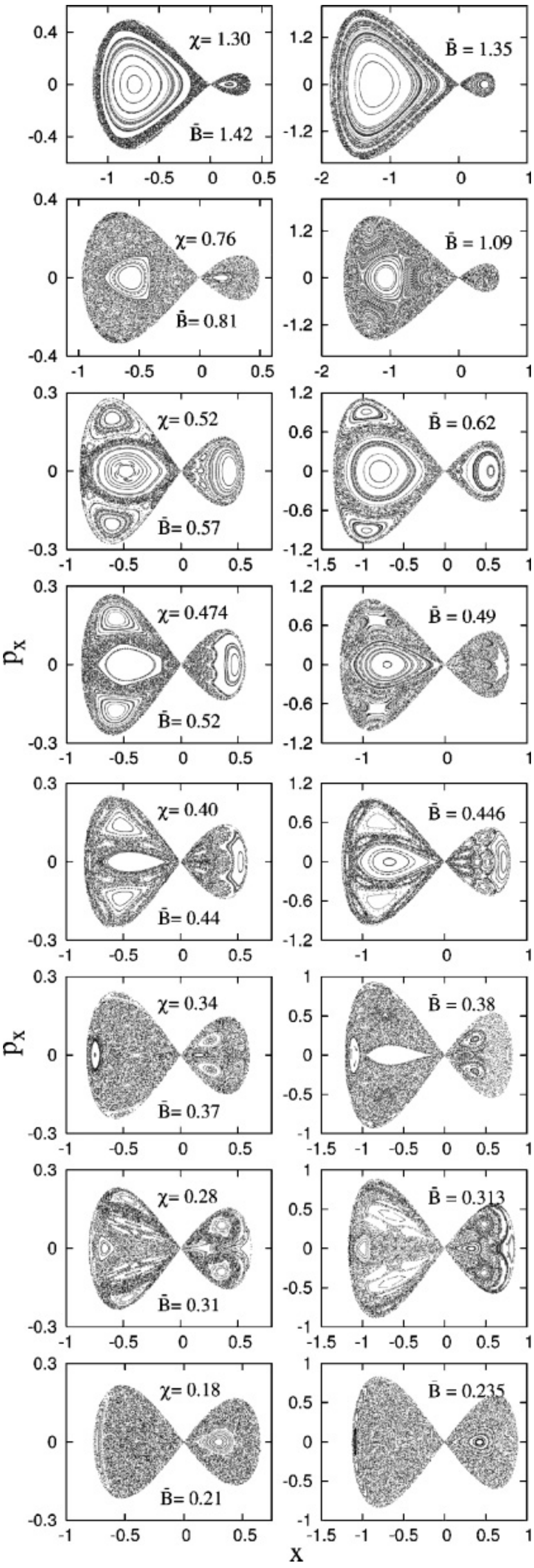

FIG. 15. Comparison of $E_{\rm cl} = 0$ Poincaré sections $y = 0$ in the IBM at $\eta = 0.75$ (lefthand column) and GCM (righthand column) at the most pronounced minima and maxima of $f_{\rm reg}(\bar{B})$ from Fig. 14.

To obtain a mapping between IBM and GCM parameters, we use scaling properties of the classical GCM Hamiltonian, see Ref. [30]. In this way, $H'_{\rm GCM}$ is transformed so that only the coefficient $\bar{B}$ in front of the term $\propto \beta^3$ remains variable while $\bar{A} = -\bar{C} = -1$ are fixed. The expression for the rescaled control parameter then reads $\bar{B}(\eta, \chi) = B'/\sqrt{|A'C'|}$. This provides the desired correspondence $(\eta, \chi) \leftrightarrow \bar{B}$ for small-amplitude vibrations (wrong scaling of the noninvariant part $H'_{\rm res}$ may then be neglected).

In Sec. III we saw that in the "middle" of the Casten triangle ($\eta = 0.5$, cf. Fig. 3) the zero-energy dependence of $f_{\rm reg}$ on $\chi$ in the IBM has the only well pronounced peak at the AW arc, quite in contrast with the corresponding fine structured $f_{\rm reg}(\bar{B})$ dependence in GCM [28] at $E_{\rm cl} = 0$ (see the inset of Fig. 14). However, as we approach the deformed-to-spherical phase transition, some significant peaks of regularity develop in the region between $\chi = 0$ and the AW arc. As the validity of approximation (19) improves in this part of the Casten triangle, the $f_{\rm reg}$ dependences start to resemble that of the GCM, see Fig. 14.

The similarity is evident also from the Poincaré sections shown in Fig. 15, where the lefthand and righthand columns correspond to the IBM and GCM, respectively. The adjacent pairs of sections belonging to the most pronounced maxima and minima of $f_{\rm reg}$ in the GCM and IBM at $\eta = 0.75$ are visually almost identical (here we use $\chi > 0$ to be consistent with the choice $B > 0$ of Refs. [28,30]). The differences must be attributed to the residual part $H'_{\rm res}$ of Hamiltonian (19), which is not obviously small.

We can conclude that the GCM peak of regularity at $\bar{B} \approx 0.6$ is closely related to the AW arc in the region $\eta \in [0.7, 0.8]$. Note, however, that the most regular IBM Poincaré section, observed at $|\chi| = 0.52$ (associated with the GCM section at $\bar{B} = 0.62$), is already deviated from the linear fit (6) of the AW arc, which predicts $|\chi_{\rm reg}| = 0.71$ for $\eta = 0.75$. This is in agreement with results of Secs. V B and VI (see Fig. 12).

## VIII. SUMMARY AND OUTLOOK

In this paper, we studied quantum and classical effects associated with a partial increase of regularity in nuclear collective dynamics away from integrable regimes. This increase seems to be a common feature of both the interacting boson model and the geometric model, but so far lacks unambiguous theoretical evidence. Below we list our most important findings together with the questions they induce:

(i) The increase of regularity, localized mainly in the absolute-energy region around $E \approx 0$, coincides with the "macroscopic" bunching of the IBM quantum states, most clearly observed in the $0^+$ spectrum. This bunching is visually similar to that observed in the O(6)-U(5) transition (see Fig. 9 and Ref. [17]), but cannot have the same origin (monodromy [18,38]) as there is no local potential maximum with the corresponding energy. More sophisticated concepts, like generalized forms of monodromy [44] or Hamiltonian fixed points [45] may turn relevant in future studies. Since the O(6)-U(5) bunching was recently related to excited-state quantum phase transitions [38], the question rises whether the present bunching induces analogous effects in the SU(3)-U(5) case.

(ii) At the classical level, the bunching pattern seems to be related to changes in stability of some specific orbits. In particular, we disclosed the crossover between orbits of types $2_{\rm a}$ and $2_{\rm b}$ from Fig. 11 and equalizing of their periods taking place in the relevant energy and parameter domains, see Fig. 13.

(iii) Proximity of the AW arc to the locus of $0_2^+$-$2_2^+$ degeneracy, previously noticed in Ref. [27], was related to the the degeneracy of $\beta$ and $\gamma$ bandheads. It remains unclear whether it is accidental or systematic. The exchange of stability of low-energy $\gamma$-vibrations [type-1 orbits from Fig. 11(a)] and $\beta$-vibrations was found to be correlated with the locus of degeneracy (see Fig. 12). It is known that no ground-state phase transition occurs in between $\gamma$-soft and $\gamma$-rigid sides of the Casten triangle, but the present observations suggest that a kind of sharp change of low-energy collective modes appears very close to the AW arc.

(iv) The relation of the AW arc to the increase of regularity observed at $E_{\rm cl} \approx 0$ in the geometric model [28] was demonstrated in the region $\eta \in [0.7, 0.8]$, i.e., close to the deformed-to-spherical transition. Even in this region, however, the IBM corrections to the GCM kinetic energy cannot be fully neglected and lead to some rescaling of the fine structure of $f_{\rm reg}$ in parameter $\bar{B}$ (see Fig. 14).

Note that findings summarized under (iii) and (iv) indicate that the semiregular arc is in fact well defined only on the deformed side of the Casten triangle [a kind of partial SU(3) dynamical symmetry being a potential explanation] and that close to the phase transition it deviates significantly from the linear fit (6).

We hope that results presented in this paper will help to eventually disclose microscopic origins of regularity in nuclear collective dynamics. This is an important fundamental task in itself, but in view of the recent revival of interest in statistical analyses of nuclear $0^+$ spectra [46] it may also turn relevant from the experimentalists' viewpoint.

## ACKNOWLEDGMENTS

M.M., P.S., and P.C. wish to thank F. Iachello for stimulating discussions and A. Frank and J. Barea for drawing the attention to the SALI method. ECT* in Trento and IKP in Cologne are acknowledged for hospitality and support. This work was funded by the Grant Agency of the Czech Republic (Project 202/06/0363), Czech Ministry of Education (Projects MSM 0021620834 and LA 080), and by German Research Foundation (Project TSE 17/1/06).

[1] F. Iachello and A. Arima, *The Interacting Boson Model* (Cambridge University Press, Cambridge, UK, 1987).
[2] A. E. L. Dieperink, O. Scholten, and F. Iachello, Phys. Rev. Lett. **44**, 1747 (1980); D. H. Feng, R. Gilmore, and S. R. Deans, Phys. Rev. C **23**, 1254 (1981).
[3] E. López-Moreno and O. Castaños, Phys. Rev. C **54**, 2374 (1996); R. F. Casten, D. Kusnezov, and N. V. Zamfir, Phys. Rev. Lett. **82**, 5000 (1999).
[4] P. Cejnar and J. Jolie, Phys. Rev. E **61**, 6237 (2000).
[5] Y. Alhassid, A. Novoselsky, and N. Whelan, Phys. Rev. Lett. **65**, 2971 (1990).
[6] Y. Alhassid and N. Whelan, Phys. Rev. C **43**, 2637 (1991).
[7] Y. Alhassid and A. Novoselsky, Phys. Rev. C **45**, 1677 (1992).
[8] Y. Alhassid and N. Whelan, Phys. Rev. Lett. **67**, 816 (1991).
[9] N. Whelan and Y. Alhassid, Nucl. Phys. **A556**, 42 (1993).
[10] N. Whelan, Ph.D. thesis, Yale University (1993).
[11] Y. Alhassid, in *Perspectives for the Interacting Boson Model*, edited by R. F. Casten *et al.* (World Scientific, Singapore, 1994), p. 591.
[12] Y. Alhassid and D. Vretenar, Phys. Rev. C **46**, 1334 (1992).
[13] V. Paar and D. Vorkapić, Phys. Lett. **B205**, 7 (1988); Phys. Rev. C **41**, 2397 (1990).
[14] V. Paar, D. Vorkapić, and A. E. L. Dieperink, Phys. Rev. Lett. **69**, 2184 (1992).
[15] T. Mizusaki, N. Yoshinaga, T. Shigehara, and T. Cheon, Phys. Lett. **B269**, 6 (1991).
[16] E. Canetta and G. Maino, Phys. Lett. **B483**, 55 (2000).
[17] S. Heinze, P. Cejnar, J. Jolie, and M. Macek, Phys. Rev. C **73**, 014306 (2006).
[18] M. Macek, P. Cejnar, J. Jolie, and S. Heinze, Phys. Rev. C **73**, 014307 (2006).
[19] M. C. Gutzwiller, *Chaos in Classical and Quantum Mechanics* (Springer, New York, 1990).
[20] H.-J. Stöckmann, *Quantum Chaos. An Introduction* (Cambridge Universty Press, Cambridge, UK, 1999).
[21] F. Haake, *Quantum Signatures of Chaos* (Springer, Berlin, 1991).
[22] P. Van Isacker, A. Frank, and J. Dukelsky, Phys. Rev. C **31**, 671 (1985); D. Kusnezov, Phys. Rev. Lett. **79**, 537 (1997); A. M. Shirokov, N. A. Smirnova, and Yu. F. Smirnov, Phys. Lett. **B434**, 237 (1998).
[23] W. M. Zhang and D. H. Feng, Phys. Rep. **252**, 1 (1995).
[24] A. Leviatan, A. Novoselsky, and I. Talmi, Phys. Lett. **B172**, 144 (1986).
[25] Y. Alhassid and A. Leviatan, J. Phys. A: Math. Gen. **25**, L1265 (1992).
[26] P. Cejnar and J. Jolie, Phys. Lett. **B420**, 241 (1998); Phys. Rev. E **58**, 387 (1998).
[27] J. Jolie, R. F. Casten, P. Cejnar, S. Heinze, E. A. McCutchan, and N. V. Zamfir, Phys. Rev. Lett. **93**, 132501 (2004).
[28] P. Cejnar and P. Stránský, Phys. Rev. Lett. **93**, 102502 (2004).
[29] P. Cejnar, M. Macek, P. Stránský, and M. Kurian, in *Capture Gamma-Ray Spectroscopy and Related Topics*, edited by A. Woehr and A. Aprahamian, AIP Conf. Proc. No. 819 (AIP, Melville, NY, 2006), p. 487.
[30] P. Stránský, M. Kurian, and P. Cejnar, Phys. Rev. C **74**, 014306 (2006).
[31] Ch. Skokos, J. Phys. A: Math. Gen. **34**, 10029 (2001); Ch. Skokos, Ch. Antonopoulos, T. C. Bountis, and M. V. Vrahatis, *ibid.* **37**, 6269 (2004).
[32] J. Jolie, R. F. Casten, P. von Brentano, and V. Werner, Phys. Rev. Lett. **87**, 162501 (2001).
[33] R. L. Hatch and S. Levit, Phys. Rev. C **25**, 614 (1982).
[34] A. Bohr and B. R. Mottelson, *Nuclear Structure*, Vol. II (Benjamin, Reading, MA, 1975).
[35] T. A. Brody, Lett. Nuovo Cimento **7**, 482 (1973).
[36] T. Guhr, J. Z. Ma, S. Meyer, and T. Wilke, Phys. Rev. D **59**, 054501 (1999).
[37] J. Jolie and S. Heinze, in [29], p. 331; M. Macek and P. Cejnar, *ibid.*, p. 570.
[38] P. Cejnar, M. Macek, S. Heinze, J. Jolie, and J. Dobeš, J. Phys. A: Math. Gen. **39**, L515 (2006).
[39] http://www-ucjf.troja.mff.cuni.cz/∼geometric.
[40] M. V. Berry and M. Tabor, Proc. R. Soc. Lond. A **349**, 101 (1976).
[41] M. C. Gutzwiller, J. Math. Phys. **12**, 34 (1971).
[42] A. Leviatan, Ann. Phys. (NY) **179**, 201 (1987).
[43] J. Dobeš, Phys. Rev. C **42**, 2023 (1990).
[44] D. A. Sadovskii and B. I. Zhilinskii, Mol. Phys. **104**, 2595 (2006).
[45] P. Leboeuf and M. Saraceno, Phys. Rev. A **41**, 4614 (1990).
[46] D. Bucurescu *et al.*, Phys. Rev. C **73**, 064309 (2006); D. Bucurescu *et al.* (unpublished).